Phonons and Static Dielectric Constant in CaTiO$_3$ from First Principles

Eric Cockayne and Benjamin P. Burton[1]

[1]*Ceramics Division, Materials Science and Engineering Laboratory,*
National Institute of Standards and Technology Gaithersburg, MD 20899-8520

CaTiO$_3$ has a static dielectric constant that extrapolates to a value greater than 300 at zero temperature. We investigate the origin of this large dielectric response on a microscopic level, using first-principles plane-wave pseudopotential density functional theory calculations. The electronic dielectric tensor and the complete set of zone center phonons and ionic Born effective charges are determined for CaTiO$_3$ in its low temperature 20-atom per cell orthorhombic phase via frozen phonon electronic structure, polarization and force constant calculations. Dispersion theory is then used to obtain the dielectric tensor. The dielectric response is dominated by low frequency ($\nu \sim 90\,\mathrm{cm}^{-1}$) polar optical modes in which cation motion opposes oxygen motion. The frequencies of these phonons, and thus the dielectric constant, are predicted to be pressure-sensitive.

PACS numbers:

I. INTRODUCTION

Ceramic solid solutions involving CaTiO$_3$ are among the candidate systems for high-quality microwave dielectric materials[1]. Pure CaTiO$_3$ has a dielectric constant of about 180 at room temperature. The dielectric constant increases monotonically as temperature decreases over the measured range from 4.2 to 430 K, and extrapolates to a value greater than 300 at zero temperature[2, 3]. Associated with the trends in dielectric constant is a large positive temperature coefficient of resonant frequency ($\tau_f \equiv \partial f/\partial T$) [4] for dielectric resonators made from CaTiO$_3$. The solid solution CaTi$_{0.54}$(Al$_{1/2}$Ta$_{1/2}$)$_{0.46}$O$_3$, however, has $\tau_f = 0$[1]. As a first step toward understanding the dielectric properties of CaTiO$_3$-based solid solutions at the microscopic level, we present a first-principles investigation of the low-temperature zero-frequency dielectric response of CaTiO$_3$.

For T $>\approx$ 1580 K, CaTiO$_3$ has the ideal perovskite structure. As temperature decreases, CaTiO$_3$ undergoes a sequence of phase transitions. Experiments have not yet pinpointed the number of phases and exact phase transition temperatures[5]. A recent powder neutron diffraction study[6] suggests that there may be as many as three phase transitions: (i) from cubic to body-centered tetragonal at T $\approx$ 1580 K, (ii) to a possible centered orthorhombic phase at T $\approx$ 1500 K, and (iii) to the low temperature primitive orthorhombic phase at T $\approx$ 1380 K. All of the structures are related to the perovskite structure via small distortions of ions from their ideal perovskite positions[6]. The structure of the low-temperature phase is shown in Figure 1. It has four CaTiO$_3$ formula units in an orthorhombic cell with $a \approx b \approx \sqrt{2}a_0$ and $c \approx 2a_0$, where a_0 is the lattice parameter of the high temperature perovskite phase. Its structure can largely be described as an oxygen-octahedron tilting structure ($a^-a^-c^+$ in Glazer's notation[7, 8]), al-though the resultant symmetry breaking also displaces Ca ions from their ideal perovskite positions.

By definition, the relative dielectric permittivity tensor of a material, $\kappa_{\alpha\beta}$, is related to its dielectric susceptibility[9]

$$\chi_{\alpha\beta} \equiv \frac{1}{\epsilon_0} \frac{\partial P_\alpha}{\partial E_\beta} \qquad (I.1)$$

via:

$$\kappa_{\alpha\beta} = \delta_{\alpha\beta} + \chi_{\alpha\beta}, \qquad (I.2)$$

where **P** is the polarization, **E** the applied electric field, and $\delta_{\alpha\beta}$ the Kronecker delta function.

It is not possible, however, to calculate the static dielectric tensor of a material in a plane-wave density functional theory calculation directly from (I.1)-(I.2), because periodic boundary conditions do not allow a finite macroscopic field. Fortunately, there exists an alternate expression for κ in terms of quantities that can be computed under zero-field boundary conditions. In the classical dispersion formula for the static dielectric tensor of a complex lattice[10],

$$\kappa_{\alpha\beta} = (\kappa_\infty)_{\alpha\beta} + \sum_{\omega_\mu^2 \neq 0} \frac{\overline{Z^\star}_{\mu\alpha}\overline{Z^\star}_{\mu\beta}}{V\epsilon_0 m_0 \omega_\mu^2}, \qquad (I.3)$$

where κ_∞ is the electronic dielectric tensor, μ labels the zone-center (**q** = 0) normal modes of the system, ω_μ their (angular) frequencies, $\overline{Z^\star}_{\mu\alpha}$ their effective charges in Cartesian direction α, V the volume per unit cell, and ϵ_0 the permittivity of free space. The mode effective charge in the α direction for a given mode μ is defined as

$$(\overline{Z^\star}_\mu)_\alpha \equiv \sum_{i\gamma} Z^\star_{i\alpha\gamma}(m_0/m_i)^{1/2}(a_\mu)_{i\gamma}, \qquad (I.4)$$
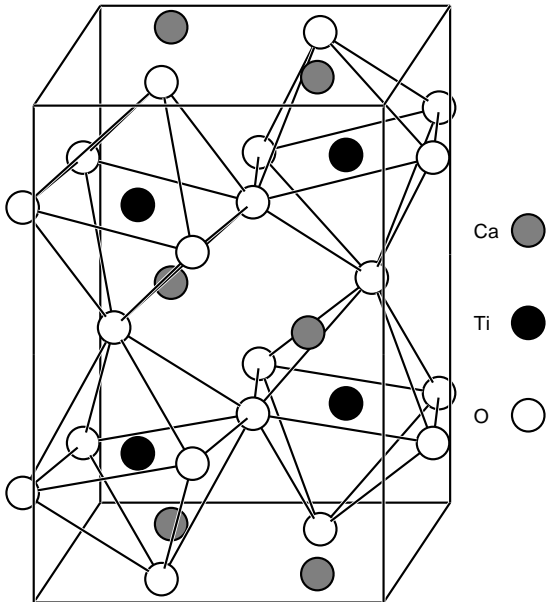
FIG. 1: Slightly-distorted perovskite experimental room-temperature structure of CaTiO$_3$. The origin of the unit cell is shifted by (–0.25,0.25,0) in cell parameters with respect to the conventional setting in order to make the TiO$_6$ octahedra more clear.

where $Z_i^\star$ is the Born effective charge tensor for ion i, m_i its mass, $(a_\mu)_{i\gamma}$ the component of the normalized dynamical matrix eigenvector for mode μ involving ion i in the γ direction, and m_0 an arbitrary mass, which is cancelled by the denominator of (I.3). We choose $m_0 = 1$ amu in this work. Finally, the components of the Born effective charge tensor for a given ion i are defined as follows:

$$Z_{i\alpha\gamma}^\star \equiv V \frac{\partial P_\alpha}{\partial u_{i\gamma}}, \qquad (\text{I.5})$$

where $\mathbf{P}$ is the polarization of the system and $u_{i\gamma}$ the motion of ion i in direction γ.

Historically, equation (I.3) has mainly found experimental applications to simple systems, such as alkali halides, for which the phonon eigenvectors are determined by symmetry[10]. Recently, optical reflectivity experiments have been used to determine the individual mode contributions to the dielectric constant in more complex systems such as Ba(B$'_{1/2}$B$''_{1/2}$)O$_3$ perovskites[11, 12] and BaMg$_{1/3}$Ta$_{2/3}$O$_3$[13, 14]. The most complex system for which this has been done has 16 infrared active modes. In its low temperature phase, CaTiO$_3$ has 25 infrared active modes, with, as we show later, widely different $\overline{Z}_\mu^\star$. It thus appears that measurement of the mode-by-mode contribution to κ in CaTiO$_3$ is at the limit of present experimental capabilities.

Even if one could measure the contribution of each mode to κ and thus each $\overline{Z}_\mu^\star$ experimentally, it is not possible to break down $\overline{Z}_\mu^\star$ into the individual phonon

eigenvectors and ionic effective charges via Eq. (I.4) without making additional assumptions (see *e.g.* Reference [12]) because Eq. (I.4) is indeterminate. First principles calculations have shown that one must be careful in making assumptions for two reasons: (1) The Born effective charges of perovskite-related materials frequently differ significantly from their nominal values[15, 16]. (2) The eigenvectors of corresponding modes in seemingly similar systems can be quite different, even in simple perovskites[17, 18]. In order to understand the origin of the dielectric behavior of CaTiO$_3$ on the microscopic level in a manner free from assumptions, we turn to first principles methods.

Lee, Ghosez, and Gonze[19] did a fully first principles calculation of the static dielectric tensor in rutile TiO$_2$, a compound with 6 atoms per unit cell and 4 sets of infrared-active modes, obtaining good agreement with experiment. In this work, we apply first-principles methods to investigate the dielectric properties of CaTiO$_3$, with 20 atoms per unit cell and 25 infrared-active modes.

II. FIRST-PRINCIPLES CALCULATIONS

All calculations are performed using VASP (the Vienna ab initio simulation package[20–23]). VASP is a code for plane-wave pseudopotential density functional theory calculations. We used ultrasoft Vanderbilt type pseudopotentials[24] as supplied by G. Kresse and J. Hafner[25]. Semicore p electrons were treated as valence electrons for the Ca and Ti pseudopotentials, but semicore s electrons were treated as core electrons. The total number of valence electrons was 8 for Ca, 10 for Ti, and 6 for oxygen. All of our calculations were done using the VASP high precision option, *i.e.* a plane-wave energy cutoff of 494.6 eV. We used the local density approximation (LDA) for the exchange-correlation energy. Brillouin zone integration was obtained by calculating Kohn-Sham wavefunctions for a set of 128 $\mathbf{k}$ points in the Brillouin zone, positioned so as to be equivalent to an $8 \times 8 \times 8$ Monkhorst-Pack grid for a primitive perovskite cell.

III. RESULTS

A Structure

There is some choice in the CaTiO$_3$ structure on which to base in the first principles dielectric calculations. First, there is the experimental structure. Various experiments report slightly different parameters for the structure of CaTiO$_3$. In Table I(A), we report the weighted average of the four structure refinements tabulated in Ref. [26]. Secondly, there is the structure obtained by fixing the cell parameters at the experimental value and performing a first-principles ionic relaxation; these parameters are shown in Table I(B). Next, one can allow both ionic

positions and cell parameters to relax under the LDA; the results are given in Table I(C). All of the first-principles relaxations were done to a convergence of better than 10^{-6} eV per formula unit, with relaxed structures used as the input for additional relaxations to make certain that the minimum was achieved. Finally, to contrast the properties of the ground state of $CaTiO_3$ with those of the high temperature perovskite structure, we present in Table I(D) the parameters for an ideal perovskite cell whose volume is the same as that of the experimental one. The ideal perovskite structure actually has a primitive five-atom cubic cell with lattice parameter 3.8245 Å.

TABLE I: Structure of $CaTiO_3$. (A) Weighted average of four room temperature structure refinements. (B) LDA ionic relaxation with same cell parameters as (A). (C) Full LDA ionic and cell relaxation. (D) Ideal perovskite with same volume as (A). Space group Pbnm, a, b, c in Å.

	A	B	C	D
a	5.3804	5.3804	5.2898	5.4086
b	5.4422	5.4422	5.4122	5.4086
c	7.6417	7.6417	7.5374	7.6490
Ca				
x	0.9935	0.9903	0.9892	0
y	0.0349	0.0443	0.0480	0
z	1/4	1/4	1/4	1/4
Ti				
x	0	0	0	0
y	1/2	1/2	1/2	1/2
z	0	0	0	0
O(1)				
x	0.0707	0.0807	0.0838	0
y	0.4842	0.4783	0.4776	1/2
z	1/4	1/4	1/4	1/4
O(2)				
x	0.7111	0.7093	0.7063	3/4
y	0.2884	0.2904	0.2927	1/4
z	0.0372	0.0427	0.0441	0

The theoretical structures generally have larger distortions from the ideal perovskite structure than the experimental ones. However, the theoretical calculation is inherently a zero-temperature calculation. Liu and Liebermann[27] report the structure parameters for $CaTiO_3$ at both 298 K and 673 K. Applying the thermal expansion factors, etc., of their results between 298 K and 673 K to linearly extrapolate the average experimental structure to zero temperature gives $a = 5.3565$, $b = 5.4316$, $c = 7.6103$, $Ca_x = 0.9921$, $Ca_y = 0.0410$, $O(1)_x = 0.0784$, $O(1)_y = 0.4839$, $O(2)_x = 0.7102$, $O(2)_y = 0.2878$, and $O(2)_z = 0.0404$. We find that roughly half of the apparent discrepancy between experimental and relaxed *ab initio* atomic positions in $CaTiO_3$ is due to the fact that the experimental results are at room temperature and not zero temperature. The rest is due both to possible systematic experimental errors due to twinning, grain boundaries, *etc.*, and to systematic er-

rors in the first-principles calculations, in particular the LDA. In fact, the full minimization leads to a cell volume that is 3.5 % less than that of the experimental volume at room temperature and 2.5 % less than that of the extrapolation of the experimental cell to zero temperature. The error in the cell parameters is about 1%, typical LDA error for perovskite oxides. The distortion of the atomic positions is slightly larger in the full LDA relaxation than the constrained one, showing an inverse correlation between cell size and amount of distortion. Full LDA relaxations predict a larger strain than is observed experimentally ($b/a = 1.019$ *vs.* 1.011 *vs.* 1.014 extrapolated low temperature). In summary, a full first-principles LDA relaxation on $CaTiO_3$ underestimates the unit cell volume by about 3%, predicts distortions of ions from their ideal perovskite positions that are about 20% larger than observed experimentally, and overestimates the anisotropic strain.

B Born effective charges

We used the King-Smith and Vanderbilt (KSV) [28] method to calculate the polarizations of perturbed cells and from this, the Born effective charge tensors of the ions. The KSV method gives the electronic contribution to polarization, to which the ionic contribution is added to obtain the total polarization $\mathbf{P}$. The component of the electronic contribution to polarization along lattice vector $\mathbf{a}_\alpha$ is computed via a set of Berry's phase calculations $\phi_{\alpha,\mathbf{k}_\perp}$ along straight-line paths in the Brillouin zone, where reciprocal lattice vector $\mathbf{b}_\alpha$ is the path vector, J the number of evenly spaced $\mathbf{k}$ points in the path, and $\mathbf{k}_\perp$ the component of $\mathbf{k}$ orthogonal to $\mathbf{b}_\alpha$ along the path. The Berry's phase is the phase of the complex product of the determinants of all wavefunction overlap matrices between successive $\mathbf{k}$ points in the path. One finally obtains

$$\mathbf{P}_{electronic} = \frac{1}{V} \sum_\alpha \frac{\overline{\Delta\phi_\alpha}}{2\pi}\mathbf{a}_\alpha(2|e|), \qquad \text{(III.1)}$$

where $\overline{\Delta\phi_\alpha}$ is the average of $\Delta\phi_{\alpha,\mathbf{k}_\perp}$ across the Brillouin zone cross section, $\Delta\phi_{\alpha,\mathbf{k}_\perp}$ being the difference between $\phi_{\alpha,\mathbf{k}_\perp}$ for the polar phase and $\phi_{\alpha,\mathbf{k}_\perp}$ for a nonpolar phase related to the polar phase by an adiabatic transformation which remains insulating. In practice, we find that $\phi_{\alpha,\mathbf{k}_\perp}$ for nonpolar phases in our calculations are easily identified as multiples of π and do not need to be explicitly calculated. See Refs. [28–30] for more details on the Berry's phase approach to polarization.

For each structure A-C, we perturbed each atom, in turn, in the x, y and z directions and calculated the charge density self-consistently via a total energy calculation. We then performed non-self-consistent wavefunction calculations in order to obtain the wavefunctions for the Berry's phase calculations. We used $J = 10$ along $\mathbf{z}$

and $J = 14$ along $\mathbf{x}$ and $\mathbf{y}$. For structure A, we obtained the cross-section average by averaging the phases for $\mathbf{k}_\perp$ on a 4×4 Monkhorst-Pack grid. To reduce computational effort for structures B and C, we only calculated wavefunctions for half the points of a 4×4 Monkhorst-Pack grid, and scaled the undetermined phases in the same average way with respect to structure A as the determined phases. For structure D, we calculated Born effective charges using a primitive cell, $J = 20$, and a centered 4×4 Monkhorst Pack grid. The grids used were necessary and sufficient to converge effective charges to about 0.02. In each case, there was a slight (order 0.01 e or less) deviation from charge neutrality in the sum of the resultant effective charge tensors due to finite difference errors. To ensure strict charge neutrality, we added a correction to each diagonal component of each ionic effective charge tensor that was proportional to the corresponding electronic contribution to the component.

The Born effective charge tensors for structures A through D are shown in Table II. The principle components of effective charges, obtained by diagonalizing the tensors, are shown in Table III, along with the corresponding results of Zhong, King-Smith and Vanderbilt for $CaTiO_3$[15] in the ideal perovskite structure. The nominal ionic charges of Ca, Ti, and O are, respectively, 2, 4, and -2. The dynamical effective charges are generally larger in magnitude than the nominal charges, especially for Ti and for O in the direction of the Ti-O bonds. These anomalously large effective charges appear to be a general feature of ABO_3 perovskites [15, 16]. The effective charges are somewhat sensitive to the structural details, generally becoming closer to their nominal ionic values with increasing deviation from the ideal perovskite structure. In previous studies, it has been found that effective charges are sensitive to polar distortions, becoming closer to their nominal values when ferroelectric relaxation occurs[16, 31–35]. This work shows that nonpolar relaxation has the same effect. While we did not study the effect of pressure independently of ionic relaxations, previous studies have shown that Born effective charges are relatively insensitive to pressure[16, 33].

There is a very good agreement between the effective charges that we found here for $CaTiO_3$ in the ideal perovskite structure and those determined by Zhong, King-Smith and Vanderbilt[15] (Table III). We suspect that the main reason for the slight discrepancies is that our calculations treat the Ti and Ca semi-core s electrons as core electrons, while they were treated as valence electrons in Zhong, King-Smith, and Vanderbilt.

In the orthorhombic $CaTiO_3$ structures, the relatively large off-diagonal components of the Ti Born effective charge tensors $Z^\star_{Ti}$ and their asymmetries were unexpected because the TiO_6 octahedra are nearly ideal. Cubic local environments imply diagonal, isotropic $Z^\star$. The large off-diagonal components of $Z^\star_{Ti}$ show that $Z^\star_{Ti}$ is not determined solely by nearest-neighbor Ti-O interactions, but is strongly influenced by further-neighbor interactions which more strongly break cubic symmetry. $Z^\star_{Ti}$ in

TABLE II: Born effective charge tensors for each of the structures shown in Table I (in $|e|$).

	A	B	C	D		A	B	C	D
$Z^\star_{Ca,xx}$	2.47	2.45	2.45	2.57	$Z^\star_{01,xx}$	–2.06	–2.07	–2.09	–2.04
$Z^\star_{Ca,xy}$	0.17	0.18	0.18	∅	$Z^\star_{01,xy}$	–0.13	–0.16	–0.17	∅
$Z^\star_{Ca,yx}$	0.15	0.14	0.15	∅	$Z^\star_{01,yx}$	0.03	0.02	0.02	∅
$Z^\star_{Ca,yy}$	2.43	2.41	2.40	2.57	$Z^\star_{01,yy}$	–1.89	–1.89	–1.87	–2.04
$Z^\star_{Ca,zz}$	2.42	2.38	2.37	2.57	$Z^\star_{01,zz}$	–5.46	–5.37	–5.35	–5.69
$Z^\star_{Ti,xx}$	6.91	6.88	6.79	7.20	$Z^\star_{02,xx}$	–3.66	–3.63	–3.58	–3.86
$Z^\star_{Ti,xy}$	0.46	0.47	0.49	∅	$Z^\star_{02,xy}$	–1.74	–1.74	–1.69	–1.82
$Z^\star_{Ti,xz}$	0.63	0.71	0.72	∅	$Z^\star_{02,xz}$	0.01	0.00	0.00	∅
$Z^\star_{Ti,yx}$	–0.57	–0.63	–0.66	∅	$Z^\star_{02,yx}$	–1.69	–1.67	–1.65	–1.82
$Z^\star_{Ti,yy}$	6.97	6.94	6.94	7.20	$Z^\star_{02,yy}$	–3.76	–3.73	–3.74	–3.86
$Z^\star_{Ti,yz}$	–0.16	–0.23	–0.23	∅	$Z^\star_{02,yz}$	–0.08	–0.09	–0.10	∅
$Z^\star_{Ti,zx}$	–0.77	–0.91	–0.90	∅	$Z^\star_{02,zx}$	0.00	0.00	0.00	∅
$Z^\star_{Ti,zy}$	–0.04	–0.06	–0.06	∅	$Z^\star_{02,zy}$	–0.06	–0.07	–0.07	∅
$Z^\star_{Ti,zz}$	6.99	6.90	6.90	7.20	$Z^\star_{02,zz}$	–1.98	–1.96	–1.96	–2.04

TABLE III: Principal components of Born effective charge tensors of Table II (in $|e|$) and comparison with results of Zhong, King-Smith, and Vanderbilt (ZKV).

	A	B	C	D	ZKV	
$Z^\star_{Ca,1}$	2.61	2.59	2.59	2.57	2.58	
$Z^\star_{Ca,2}$	2.42	2.38	2.37	2.57	2.58	
$Z^\star_{Ca,3}$	2.29	2.27	2.26	2.57	2.58	
$Z^\star_{Ti,1}$	7.07	7.06	7.06	7.20	7.08	
$Z^\star_{Ti,2}$	6.95*	6.90*	6.86*	7.20	7.08	
$Z^\star_{Ti,3}$	6.95*	6.90*	6.86*	7.20	7.08	*Modulus of
$Z^\star_{01,1}$	–5.46	–5.37	–5.35	–5.69	–5.65	
$Z^\star_{01,2}$	–2.03	–2.05	–2.07	–2.04	–2.00	
$Z^\star_{01,3}$	–1.92	–1.91	–1.89	–2.04	–2.00	
$Z^\star_{02,1}$	–5.43	–5.38	–5.33	–5.69	–5.65	
$Z^\star_{02,2}$	–2.03	–2.02	–2.03	–2.04	–2.00	
$Z^\star_{02,3}$	–1.93	–1.91	–1.91	–2.04	–2.00	

complex eigenvalue

all of the orthorhombic structures is so asymmetric that two of its eigenvalues are *complex*. For these eigenvalues, we report the modulus in Table III.

C Electronic dielectric tensor

To calculate the electronic contribution to the dielectric tensors, we used a modification of the method of Bernardini, Fiorentini, and Vanderbilt (BFV)[36, 37]. In the BFV method, an artificial supercell of a homogeneous nonpolar material extended in the α direction is created, where the half of the cell with $x_\alpha < 0.5$ is given *ionic* polarization $\mathbf{P}_1^{(0)}$ and the half of the cell with $x_\alpha > 0.5$ is given *ionic* polarization $\mathbf{P}_2^{(0)}$ by small displacements of the ions in each half.

By applying classical electrostatics to the "interface" charge density at $x_\alpha = 0.5$, σ, BFV obtained a formula for the electronic dielectric tensor components (for the

case of diagonal κ_∞, such as for orthorhombic CaTiO$_3$):

$$(\kappa_\infty)_{\alpha\alpha} = \frac{P_{1\alpha}^{(0)} - P_{2\alpha}^{(0)}}{\sigma}. \qquad \text{(III.2)}$$

In practice, we have found that it is difficult to determine σ unambiguously, because it is spread out over atomic dimensions along α and because it is small relative to the fluctuations of charge density due to the atomicity of the material. Instead, we used the energy of the Ti semicore 2p electrons orthogonal to the macroscopic field as a "probe" of the local potential. By calculating the difference of Ti 2p electron energies on different planes, we determined the macroscopic electric fields $E_{1\alpha}$ and $E_{2\alpha}$, and from $E_{1\alpha}$ and $E_{2\alpha}$, used

$$(\kappa_\infty)_{\alpha\alpha} = \frac{P_{1\alpha}^{(0)} - P_{2\alpha}^{(0)}}{\epsilon_0(E_{2\alpha} - E_{1\alpha})} \qquad \text{(III.3)}$$

to obtain κ_∞.

In detail, we created 40 atom supercells from the 20 atom CaTiO$_3$ cells A-D by doubling in each of the $\alpha = x$, y and z directions. Then we moved each ion in the original cell in the α direction by $0.001a/(Z_{i\alpha\alpha}^\star)$ (a = 3.8245 Å) and each ion in the second cell by $-0.001a/(Z_{i\alpha\alpha}^\star)$, using the values of $Z_i^\star$ found in Section III. B, in order to make the polarizations in the two layers equal, in opposite directions, and as uniform as possible. We found that the local field converges rapidly with supercell size, and already within 1% for our double supercells.

The results for electronic dielectric tensor are shown in Table IV. The values are within 10% for the different structures, decreasing as the distortion from the ideal perovskite structure increases. Previous studies have shown that *polar* distortions tend to decrease κ_∞[32–34]; here we find that nonpolar distortions have the same effect. The experimental value is $\kappa_\infty = 5.81$[15], compared to our value of 6.12 for CaTiO$_3$ in its experimental structure. It is typical for LDA calculations to overestimate κ_∞ slightly. Fiorentini and Bernardini report $\kappa_\infty = 5.87$ for CaTiO$_3$ in its ideal perovskite structure, using their method, much closer to its experimental value, but they do not report the lattice parameter used.

TABLE IV: Electronic dielectric tensor for each of the structures shown in Table 1.

	A	B	C	D
κ_{xx}	6.06	6.03	5.64	6.19
κ_{yy}	6.05	6.02	5.64	6.19
κ_{zz}	6.26	6.19	6.06	6.19
$(\kappa_{xx} + \kappa_{yy} + \kappa_{zz})/3$	6.12	6.08	5.78	6.19

D Phonons

After calculating the residual Hellmann-Feynman forces on each structure in Table I, we displaced each ion in turn in each Cartesian direction by ± 0.01 Å and recalculated the forces. From finite differences, we determined the force constants matrices. We diagonalized the corresponding dynamical matrices to obtain the normal mode frequencies and eigenvectors.

The phonon spectra for structures A-C are shown in Tables V- IX. Each table gives the spectra for one or more irreducible representations (irreps) of the point group of CaTiO$_3$. The mode effective charges, as defined in Eq. I.4, are given for each infrared active (polar) mode in tables V- VII.

The phonon frequencies are similar for the different structures. The root mean square variation between corresponding phonon frequencies with the same irrep for the different structures varies between 13 and 40 cm^{-1}. The phonon frequencies generally increase with pressure (compare structure C with structures A and B), as is observed experimentally[38], and as is expected, since short-range repulsion between ions increases as the distance between them decreases.

The distortion of the CaTiO$_3$ ground state structure from the ideal perovskite structure projects entirely onto modes with irrep A_g in the orthorhombic phase. These modes stiffen significantly as the ions relax to their LDA ground state, with fixed cell parameters, going from structure A to structure B. There is a particularly good agreement between the phonon frequencies of the infrared modes of structures A and B; thus the anharmonic coupling of the A_g modes to the infrared-active modes is relatively small.

For every infrared-active irrep in structure A and B, the mode with the highest effective charge has the lowest frequency. By projecting the eigenvectors onto the normal mode eigenvectors of CaTiO$_3$ in its ideal perovskite structure, we find that these modes are closely associated with the $140i$ cm^{-1} ferroelectric instability of CaTiO$_3$. CaTiO$_3$ is nonpolar rather than ferroelectric, because competing, stronger, octahedron-tilting instabilities at the M and R points freeze in first. Anharmonic coupling stabilizes the would-be ferroelectric instability and no ferroelectric phase transition occurs in CaTiO$_3$. For structure C, there are no longer single modes within any infrared-active irrep in which $\overline{Z_\mu^\star}$ clearly dominates; rather there is a pair of relatively-low frequency modes with $\overline{Z_\mu^\star} \approx 2$. The would-be ferroelectric instability is very sensitive to pressure in CaTiO$_3$ and significant eigenvector mixing occurs at the pressures of structure C.

Our analysis of the polar Γ point mode frequencies agrees well with previous work by Zhong, King-Smith, and Vanderbilt[15] (Table X), and we have extended their results by determining the frequency of the nonpolar Γ_{25} mode and all the modes at the X, M and R points. We find both a ferroelectric instability of the perovskite structure and octahedral tilting instabilities at both M and R. Instabilities have been found for *all* perovskite titanate systems studied to date[18, 39]. Systematic trends in the instabilities with increasing lattice parameter can
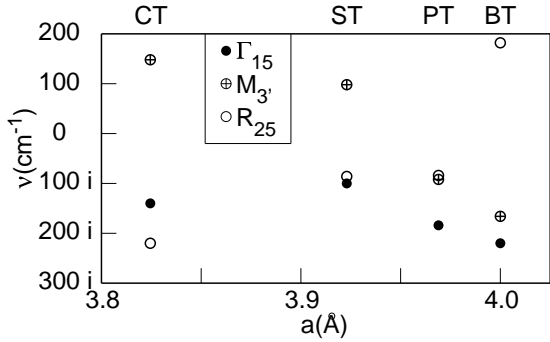
FIG. 2: Comparison of soft modes in the perovskite titanates CaTiO$_3$, SrTiO$_3$, PbTiO$_3$, and BaTiO$_3$. All results are from first principles calculations on materials with the ideal perovskite structure. Imaginary frequencies indicate harmonic instabilities. The data for PbTiO$_3$ and BaTiO$_3$ are compiled in [18]. The data for SrTiO$_3$ are reported in [39]. The data for CaTiO$_3$ are from the present study.

be identified. For example, the soft modes involving Ti motion against O along the Ti-O chains, such as the softest antiferroelectric $M_{3'}$ mode, tend to become more unstable as the lattice parameter increases (see Figure 2). The octahedral tilting modes (e.g. R_{25}) tend to become more stable. The trend in the ferroelectric Γ_{15} instability is not monotonic with size; however we do find a trend in the nature of the ferroelectric instability *eigenvector*. The normalized ferroelectric instability dynamical matrix eigenvector for perovskite CaTiO$_3$ is (Ca,Ti,O$_\perp$,O$_\perp$, O$_\parallel$) = (0.6338,0.1535,–0.5027,–0.5027,–0.2632). By comparison with the other perovskite systems for which the ferroelectric eigenvector has been reported[18], we find that the Ti and O motion along Ti-O bonds (O$_\parallel$) increases as the lattice parameter increases, and the A cation and transverse O motion (O$_\perp$) decreases.

A number of studies have reported infrared[38, 40] and Raman[38, 41–43] spectra for CaTiO$_3$. Interpretation of the data is difficult because, as Table VIII shows, there are so many Raman-active modes in CaTiO$_3$ that significant overlap between peaks is expected. Furthermore, the relative intensity of different Raman peaks in CaTiO$_3$ is very sensitive to temperature[38]. Because the experimental peak intensity is sensitive to temperature and because we did not calculate theoretical Raman scattering strengths, we will not attempt here to correlate predicted and measured Raman frequencies.

Perry *et al.* interpreted infrared reflectivity measurements on CaTiO$_3$ in terms of two polar phonon triplets at 148 cm^{-1} and 178 cm^{-1} and a split triplet at 443 cm^{-1} and 549 cm^{-1}. A material with an ideal perovskite structure has three polar phonon triplets. Although symmetry analysis of the orthorhombic CaTiO$_3$ phase yields 25 polar phonon singlets, if the distortion from the ideal perovskite structure is small, there should be three pseudotriplets of phonons with large $\overline{Z^\star}$. By studying the evo-

lution of the interpolated dynamical matrix eigenmodes as the structure is distorted from from structure D to structures A, B, and C, we find that the ideal perovskite 625 cm^{-1} polar mode evolves to a pseudotriplet of modes in the 500-550 cm^{-1} range in each case. For structure A, the pseudotriplet of modes at 88-94 cm^{-1} emanates from the 140i cm^{-1} ferroelectric instability, while the 151-174 cm^{-1} pseudotriplet emanates from the ideal perovskite 200 cm^{-1} modes. For structures B and C, there is increasing mixing among the low-frequency sets of modes. By comparing the results of Perry et al. with our calculations for structure A, we conclude that: The experimental 549 cm^{-1} peak corresponds to the pseudotriplet in the 519-536 cm^{-1} range. The experimental 443 cm^{-1} peak corresponds to the calculated medium-$\overline{Z^\star}$ peaks in the 423-434 cm^{-1} range with B_{1u} and B_{3u} symmetry, which are actually most closely associated with the antiferroelectric Ti-motion 460 cm^{-1} $R_{25'}$ mode of the ideal perovskite structure. The 148 cm^{-1} and 179 cm^{-1} experimental peaks actually correspond to peaks in the same pseudotriplet. Finally, there is a calculated pseudotriplet in the 85 to 104 cm^{-1} range with very large $\overline{Z^\star}$ which was not observed experimentally. There is some discrepancy between the predicted and measured frequencies. Whether this is due to finite temperature effects or LDA errors remains to be seen.

Finally, the contribution of each infrared active mode to the static dielectric tensor is given in tables V-VII, using equation (I.3) with $\omega_\mu = 2\pi\nu_\mu$. The total static dielectric tensor, obtained by summing up the mode contributions and the electronic dielectric tensor, are given in Table XI. Table XI also gives the "average dielectric constant" for the material, $\frac{1}{3}(\kappa_{xx} + \kappa_{yy} + \kappa_{zz})$, which is the dielectric constant that one would measure for an ideal ceramic sample of a material with an anisotropic dielectric tensor. These values range from 100 for structure C to 275 for structure B.

TABLE V: Normal modes frequencies (in cm^{-1}), effective charges (in $|e|$), and contribution to dielectric susceptibility for infrared-active modes with irreducible representation B_{1u} of point group D_{2h} for structures A, B and C of Table I.

| | A | | | B | | | C | |
ν	$\overline{Z^\star}_z$	$(\kappa_\mu)_{zz}$	ν	$\overline{Z^\star}_z$	$(\kappa_\mu)_{zz}$	ν	$\overline{Z^\star}_z$	$(\kappa_\mu)_{zz}$
0	0	0	0	0	0	0	0	0
94	2.67	176	87	2.84	236	129	1.11	17
122	0.17	0	112	1.31	30	157	2.08	40
174	1.96	28	171	1.19	11	202	2.10	25
240	0.17	0	251	0.39	1	283	0.59	1
428	0.65	1	423	0.74	1	438	0.84	1
490	0.06	0	468	0.04	0	501	0.06	0
530	1.63	2	508	1.36	2	540	1.63	2

TABLE VI: Same as Table V, for B_{2u} modes.

ν	$\overline{Z^\star}_y$	$(\kappa_\mu)_{yy}$	ν	$\overline{Z^\star}_y$	$(\kappa_\mu)_{yy}$	ν	$\overline{Z^\star}_y$	$(\kappa_\mu)_{yy}$
	A			B			C	
0	0	0	0	0	0	0	0	0
88	2.99	253	104	3.10	197	145	2.30	57
157	1.35	16	161	1.29	14	183	2.11	30
195	0.59	2	217	0.38	1	238	0.50	1
233	0.14	0	250	0.55	1	268	0.54	1
290	0.75	1	294	0.75	1	314	1.13	3
320	0.11	0	332	0.18	0	362	0.17	0
485	0.22	0	480	0.47	0	496	0.25	0
519	1.54	2	505	1.20	1	529	1.50	2
547	0.05	0	546	0.12	0	565	0.06	0

TABLE VII: Same as Table V, for B_{3u} modes.

ν	$\overline{Z^\star}_x$	$(\kappa_\mu)_{xx}$	ν	$\overline{Z^\star}_x$	$(\kappa_\mu)_{xx}$	ν	$\overline{Z^\star}_x$	$(\kappa_\mu)_{xx}$
	A			B			C	
0	0	0	0	0	0	0	0	0
89	2.78	216	85	3.15	298	141	2.41	67
151	1.74	29	160	0.94	8	175	1.94	28
191	0.07	0	199	0.50	1	221	0.53	1
245	0.12	0	271	0.01	0	286	0.04	0
292	0.58	1	311	0.64	1	331	0.80	1
345	0.36	0	362	0.29	0	386	0.35	0
434	0.68	1	424	0.80	1	447	0.96	1
484	0.01	0	483	0.04	0	495	0.07	0
536	1.46	2	525	1.24	1	549	1.36	1

TABLE VIII: Frequencies (in cm^{-1}) for Raman active normal modes. Second row gives irreducible representations

A				B				C			
A_g	B_{1g}	B_{2g}	B_{3g}	A_g	B_{1g}	B_{2g}	B_{3g}	A_g	B_{1g}	B_{2g}	B_{3g}
ν	ν	ν	ν	ν	ν	ν	ν	ν	ν	ν	ν
100	137	155	174	140	177	189	184	158	193	206	206
139	162	224	325	168	189	226	327	182	206	239	340
225	195	342	439	243	219	348	444	265	241	371	459
268	346	512	518	290	354	494	496	306	373	532	540
314	431	746	807	337	438	718	783	361	455	757	816
446	469			447	476			465	493		
533	774			515	753			551	782		

TABLE IX: Frequencies (in cm^{-1}) for normal modes with irreducible representation A_u. These modes are neither infrared nor Raman active.

A	B	C
ν	ν	ν
119	107	125
135	122	156
142	140	164
178	194	213
266	274	292
426	421	439
472	439	484
510	498	522

IV. DISCUSSION

The measured dielectric constant of $CaTiO_3$ in the limit of zero temperature ranges from about 330 for a ceramic sample[3] to greater than 350 for a single crystal (of undetermined orientation)[2]. The experimental results are about 30% greater than the calculated results for structures A and B, based on the experimental lattice parameters, but more than three times the calculated dielectric constant of 100 for the fully-relaxed LDA structure. Clearly, first principles calculations do a better job predicting the dielectric constant if the experimental lattice parameters are used rather than the LDA lattice parameters. The remaining discrepancies between computed and measured dielectric constants can be explained by LDA errors in force constants. By modifying the force constant matrices for structures A and B and recomputing the dielectric constants, we find that errors as small as 5% in the force constants involving bonding along Ti-O chains can account for the 30% difference between the computed and measured dielectric constants.

The calculated average stress on structure B, with LDA ionic relaxation and experimental lattice parameters, is -6.75 GPa. Adjusting the external pressure to correct for the LDA volume error, structure C is the predicted structure of $CaTiO_3$ under 6.75 GPa pressure, and we predict that the dielectric constant of $CaTiO_3$ will decrease to about 100 at this pressure.

The dielectric constant is predicted to be sensitive to pressure, but less sensitive to nonpolar relaxation, as can be seen by the small difference in dielectric constant between structures A and B. For single crystals, we predict an anisotropy in dielectric constant along different axes that is of order 30-40%, an effect that has yet to be investigated experimentally. The axis of largest dielectric constant does depend on the details of the structure, being in the y direction for structure A and the x direction for structure B.

The ability of first principles to reproduce the large experimental dielectric constant of $CaTiO_3$ to within 30% allows the microscopic origin of this large dielectric constant to be determined. Normal mode analysis shows that 85-90% of the dielectric constant magnitude is due to a single pseudotriplet of modes with $\nu \sim 90$ cm^{-1} and large $\overline{Z^\star}$. The large $\overline{Z^\star}$ of these modes is due both to anomalously large ionic Born effective charges in $CaTiO_3$ (if the dynamical charges had their nominal values, κ would be only about 100 for structures A and B), and the nature of the phonon eigenvector, which involves significant motion of all ions, with cation motion opposing oxygen motion (see Figure 3). Decrease of κ with pressure is due to the hardening of the low-frequency phonons with pressure, but the magnitude of $\overline{Z^\star}$ for the lowest frequency modes also decreases significantly.

Experimentally, κ in $CaTiO_3$ decreases rapidly with temperature, with a value of 170-190 at room

TABLE X: Frequencies (in cm^{-1}) for ideal perovskite $CaTiO_3$ normal modes. Full results for high symmetry points in the Brillouin zone are given in columns. For a given point, phonons are grouped by irreducible representation. A, TO, and LO indicate acoustic, transverse optical, and longitudinal optical, respectively. Values in parentheses for Γ are those reported by Zhong, King-Smith and Vanderbilt[15].

$\Gamma_{15}(A)$	0	X_1	270	M_1	440	$R_{2'}$	913
$\Gamma_{15}(TO)$	140 i (153 i)	X_1	538	M_2	620	$R_{12'}$	592
$\Gamma_{15}(TO)$	200 (188)	$X_{2'}$	203	$M_{2'}$	70	R_{15}	86
$\Gamma_{15}(TO)$	625 (610)	$X_{2'}$	836	M_3	207 i	R_{15}	426
$\Gamma_{15}(LO)$	136 (133)	X_3	201	$M_{3'}$	148	R_{25}	219 i
$\Gamma_{15}(LO)$	428 (427)	X_5	81	$M_{3'}$	591	$R_{25'}$	460
$\Gamma_{15}(LO)$	864 (866)	X_5	159	M_4	878		
Γ_{25}	130	X_5	608	M_5	278		
		$X_{5'}$	20	$M_{5'}$	48 i		
		$X_{5'}$	283	$M_{5'}$	238		
				$M_{5'}$	505		

TABLE XI: Phonon contribution to, and total static dielectric tensor ($\kappa = \kappa_\infty + \kappa_{phonon}$) for structures A-C.

	A	B	C
$(\kappa_{phonon})_{xx}$	249	310	100
$(\kappa_{phonon})_{yy}$	275	216	95
$(\kappa_{phonon})_{zz}$	207	279	85
κ_{xx}	255	316	106
κ_{yy}	281	222	100
κ_{zz}	214	286	91
$(\kappa_{xx} + \kappa_{yy} + \kappa_{zz})/3$	250	275	99

temperature[2, 3]. In fact, the dielectric constant as a function of temperature follows a Curie-Weiss law appropriate for an "incipient ferroelectric" with a negative T_c[3, 44]. First-principles effective Hamiltonians based on projecting the ionic degrees of freedom of ferroelectrics to those responsible for the ferroelectric phase transition[45] correctly reproduce their Curie-Weiss dielectric behavior[46, 47]. This suggests that a similar approach be applied to computing the temperature dependence of the dielectric response of $CaTiO_3$. For a successful effective Hamiltonian approach to dielectric behavior, it is necessary that the bulk of the dielectric response be due to a set of soft modes emanating a subspace of normal modes of the ideal perovskite structure which is invariant under cubic symmetry. This is indeed the case for $CaTiO_3$, where most of the dielectric behavior is due to a pseudotriplet of modes which emanate from a Γ_{15} instability of the ideal perovskite structure. The situation in $CaTiO_3$ is complicated, however, by the competing octahedron tilting instabilities which give rise to the observed structural phase transitions, as well as the coupling of these modes to the soft polar modes. A previous attempt to derive an effective Hamiltonian for $CaTiO_3$ in terms of ferroelectric and octahedral tilting instabilities
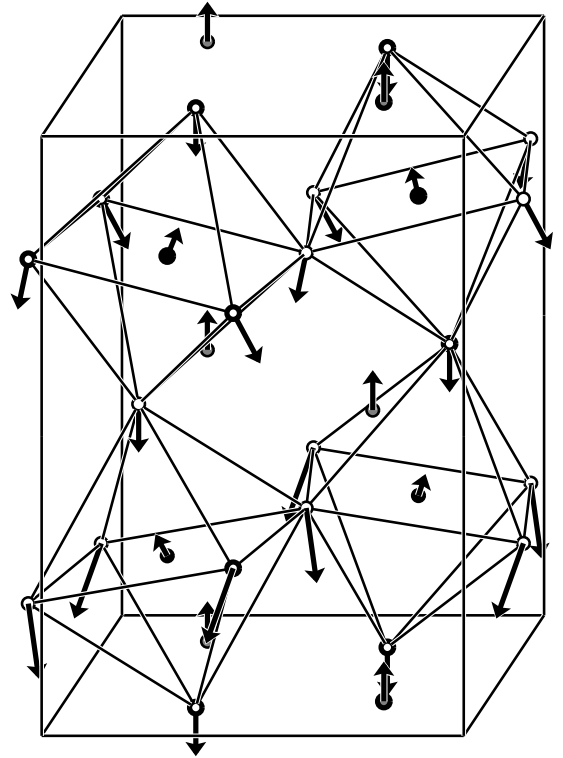

FIG. 3: Eigenvector for 94 cm^{-1} B_{1u} mode of structure A

and their coupling to each other resulted in a model[48] which did not correctly reproduce the observed ground state, probably due to the lack of sufficient anharmonic terms in the Hamiltonian. Nonetheless, with sufficient anharmonic terms, the use of the effective Hamiltonian method to calculate the temperature dependence of the dielectric properties of $CaTiO_3$ should be straightforward in principle, if complicated in detail.

V. CONCLUSIONS

We have used first-principles methods to successfully compute the low-temperature phonon and dielectric properties of $CaTiO_3$. Using dispersion theory, we relate the dielectric properties to the phonon properties and have shown that the large dielectric constant in $CaTiO_3$ is mainly due to a pseudotriplet of low frequency phonons with large mode effective charge. First-principles classification of phonon properties is ideally suited for investigating the microscopic physical origin of the dielectric constant of systems with complex structures where experimental determination of phonon properties is difficult.

VI. ACKNOWLEDGEMENTS

REFERENCES

[1] S. Kucheiko, J.-W. Choi, H.-J. Kim, and H.-J. Jung, *J. Am. Ceram. Soc.* **79**, 2739 (1996).

[2] A. Linz Jr. and K. Herrington, *J. Chem. Phys.* **28**, 824 (1958).

[3] V. V. Lemanov, A. V. Sotnikov, E. P. Smirnova, M. Weihnacht, and R. Kunze, *Solid State Comm.* **110**, 611 (1999).

[4] R. C. Kell, A. C. Greenhaum, and G. C. E. Olds, *J. Am. Ceram. Soc.* **56**, 352 (1973).

[5] T. Matsui, H. Shigematsu, Y. Arita, Y. Hanajiri, N. Nakamitsu, and T. Nagasaki, *J. Nucl. Mater.* **247**, 72 (1997), and references therein.

[6] B. J. Kennedy, C. J. Howard, and B. C. Chakoumakos, *J. Phys.: Condens. Matter* **11**, 1479 (1999).

[7] A. M. Glazer, *Acta Cryst.* **B28**, 3384 (1972).

[8] T. Vogt and W. W. Schmahl, *Europhys. Lett.* **24**, 281 (1993).

[9] We use SI units for all equations in this work.

[10] M. Born and K. Huang, "Dynamical Theory of Crystal Lattices" (Oxford: Oxford University Press), 1954. Equation (3) in this work corresponds to equation (33.28) of Born and Huang.

[11] J. Petzelt, R. Zurmühlen, A. Bell, S. Kamba, G. V. Kozlov, A. A. Volkov, and N. Setter, *Ferroelectrics* **133**, 205 (1992).

[12] R. Zurmühlen, J. Petzelt, S. Kamba, V. V. Voitsekhovskii, E. Colla, and N. Setter, *J. Appl. Phys.* **77**, 5341 (1995).

[13] D. A. Sagala and S. Koyasu, *J. Am. Ceram. Soc.* **76**, 2433 (1993).

[14] M. Furuya, *J. Appl. Phys.* **85**, 1084 (1999).

[15] W. Zhong, R. D. King-Smith, and D. Vanderbilt, *Phys. Rev. Lett.* **72**, 3618 (1994).

[16] Ph. Ghosez, J.-P. Michenaud, and X. Gonze, *Phys. Rev. B* **58**, 6224 (1998).

[17] R. E. Cohen and H. Krakauer, *Ferroelectrics* **136**, 65 (1992).

[18] Ph. Ghosez, E. Cockayne, U. V. Waghmare and K. M. Rabe, *Phys. Rev. B* **60**, 836 (1999).

[19] C. Lee, Ph. Ghosez, and X. Gonze, *Phys. Rev. B* **50**, 13379 (1994).

[20] G. Kresse and J. Hafner, *Phys. Rev. B* **47**, RC558 (1993).

[21] G. Kresse, Thesis, Technische Universität Wien, 1993.

[22] G. Kresse and J. Furthmüller, *Comput. Mat. Sci.* **6**, 15 (1996).

[23] G. Kresse and J. Furthmüller, *Phys. Rev. B* **54**, 11169 (1996).

[24] D. Vanderbilt, *Phys. Rev. B* **41**, 7892 (1990).

[25] G. Kresse and J. Hafner, *J. Phys.: Condens. Matter* **6**, 8245 (1994).

[26] A. R. Chakhmouradian and R. H. Mitchell, *J. Solid State Chem.* **138**, 272 (1998).

[27] X. Liu and R. C. Liebermann, *Phys. Chem. Minerals* **20**, 171 (1993).

[28] R. D. King-Smith and D. Vanderbilt, *Phys. Rev. B* **47**, 1651 (1992).

[29] R. Resta, *Rev. Mod. Phys.* **66**, 899 (1994).

[30] D. Vanderbilt and R. D. King-Smith, "Electronic polarization in the ultrasoft pseudopotential formalism", unpublished preprint (http: //www.physics.rutgers.edu / dhv /preprints /index.html).

[31] Ph. Ghosez, X. Gonze, Ph. Lambin, and J.-P. Michenaud, *Phys. Rev. B* **51**, 6765 (1995).

[32] C.-Z. Wang, R. Yu, and H. Krakauer, *Phys. Rev. B* **54**, 11161 (1996).

[33] Ph. Ghosez, X. Gonze, and J.-P. Michenaud, *Ferroelectrics* **194**, 39 (1997).

[34] E. Cockayne and K. M. Rabe, *Phys. Rev. B* **56**, 7947 (1997).

[35] L. Bellaiche, J. Padilla, and D. Vanderbilt, in *First Principles Calculations for Ferroelectrics: Fifth Williamsburg Workshop (AIP Conference Proceedings 436)*, Woodbury, NY: American Institute of Physics (1998), p. 11.

[36] F. Bernardini, V. Fiorentini, and D. Vanderbilt, *Phys. Rev. Lett.* **79**, 3958 (1997).

[37] F. Bernardini and V. Fiorentini, *Phys. Rev. B* **58**, 15292 (1998).

[38] P. Gillet, F. Guyot, G. D. Price, B. Tournerie, and A. L. Cleach, *Phys. Chem. Minerals* **20**, 159 (1993).

[39] C. LaSota, C.-Z. Wang. R. Yu, and H. Krakauer, *Ferroelectrics* **194**, 109 (1997).

[40] C. H. Perry, B. N. Khanna, and G. Rupprecht, *Phys. Rev.* **135**, A408 (1964).

[41] U. Balachandran and N. G. Eror, *Solid State Comm.* **44**, 815 (1982).

[42] P. McMillan and N. Ross, *Phys. Chem. Minerals* **16**, 21 (1988).

[43] P. Gillet, G. Fiquet and I. Daniel, *Geophys. Res. Lett.* **20**, 1931 (1993).

[44] G. Rupprecht and R. O. Bell, *Phys. Rev.* **135**, A748 (1964).

[45] U. V. Waghmare and K. M. Rabe, *Phys. Rev. B* **55**, 6161 (1997).

[46] K. M. Rabe and E. Cockayne, in *First Principles Calculations for Ferroelectrics: Fifth Williamsburg Workshop (AIP Conference Proceedings 436)*, Woodbury, NY: American Institute of Physics

(1998), p. 61.

[47] A. García and D. Vanderbilt, in *First Principles Calculations for Ferroelectrics: Fifth Williamsburg Workshop (AIP Conference Proceedings 436)*, Woodbury, NY: American Institute of Physics

(1998), p. 53.

[48] D. Vanderbilt and W. Zhong, *Ferroelectrics* **206**, 181 (1998).